JOURNAL OF MECHANICAL ENGINEERING AND SCIENCES
ISSN: 2289-4659 e-ISSN: 2231-8380
VOLUME 20, ISSUE 3, 2026, 11276 - 11288
DOI: https://doi.org/10.15282/jmes.20.3.2026.1.0878

RESEARCH ARTICLE

Hydrodynamic mechanisms of jet mixing-induced cooling enhancement for reactor thermal stability using an experimental-CFD approach

Nadia Kamarrudin[1,2,4], Masli Irwan Rosli[2]* and Mohd Sobri Takriff[3]

[1]Faculty of Chemical Engineering, Universiti Teknologi MARA (UiTM), Shah Alam 40450, Malaysia
[2]Faculty of Engineering and Built Environment, Universiti Kebangsaan Malaysia, 43600, Bandar Baru Bangi Selangor, Malaysia
[3]Chemical and Water Desalination Engineering Program, College of Engineering, University of Sharjah, P.O.Box 27272 Sharjah, United Arab Emirates
[4]Surface Coating Research Group, Faculty of Chemical Engineering, Universiti Teknologi MARA (UiTM), Shah Alam 40450, Malaysia

Abstract – Thermal runaway is a severe process safety hazard, particularly in stirrerless reactors, where the absence of mechanical agitation limits heat redistribution under abnormal operating conditions. Jet mixing cooling combines coolant injection with internal circulation; however, the hydrodynamic mechanisms by which jet configuration influences the transient thermal response remain insufficiently characterized. This study integrates experiments and Computational Fluid Dynamics (CFD) to examine jet Reynolds number (Re_j) effects for a 45° side jet and 90° axial bottom jet in a cylindrical vessel (0.16 m in diameter and 0.24 m in liquid height). Experiments were conducted at Re_j = 3828, 4290, 4752, and 5148. After validation, the CFD analysis was extended to Re_j = 5610 and 5808. The CFD model was validated for the representative 90° axial bottom jet at two thermocouple locations, with average relative errors of 0.91% at TC1 and 0.88% at TC2. Increasing Re_j reduced t_{50} and t_{90} by approximately 35% to 36% for both configurations. At the same Re_j, the axial bottom jet reduced t_{50} by 7.2% to 8.1% and t_{90} by 3.8% to 5.5% relative to the side jet, consistently providing better cooling performance. The CFD fields show that increasing Re_j increases transport intensity, whereas jet orientation determines how momentum is organized within the vessel. The axial jet develops symmetric recirculation throughout the vessel depth, whereas the side jet produces an asymmetric circulation pathway. The results establish how jet momentum and hydrodynamic structure influence transient cooling and provide practical guidance for stirrerless reactor cooling systems during thermal excursions.

Article History
Received : 2 April 2026
Revised : 20 July 2026
Accepted : 14 September 2026
Published : 30 September 2026

Keywords
CFD
Jet mixing
Reynolds number
Cooling enhancement
Hydrodynamic mechanism
Reactor thermal stability

1. Introduction

Process safety is a fundamental concern throughout the design and operation of chemical production processes, and thermal runaway is among the most severe failure modes. Thermal runaway occurs when heat generation exceeds heat removal, causing the reactor temperature to increase progressively. As reaction rates often increase with temperature, heat release can accelerate, and the available response time can decrease rapidly [1]-[2]. Balasubramanian and Louvar [3] reported that approximately 26% of major petrochemical accidents were associated with thermal runaway, while Dakkoune et al. [4] identified a comparable proportion of about 25% for the French chemical industry. Such events can have serious consequences, including product degradation, equipment damage, vessel rupture, and toxic release [5]-[6]. Conventional control and protection systems can reduce this risk, but their effectiveness may be challenged during rapid thermal excursions or abnormal operating conditions [7]-[9]. The effectiveness of thermal control during thermal excursion also depends on adequate internal circulation. Although mechanical agitated reactors are widely used in liquid-phase processing, the unagitated condition remains directly relevant to industrial reactor safety. Some process and storage vessels operate without mechanical agitation. Normally agitated reactors may also become effectively unagitated following agitator failure, power loss, mechanical damage, or emergency shutdown [10]-[11]. This can increase the risk of poor heat redistribution during thermal excursions. Conventional reactor cooling commonly relies on cooling jackets, internal coils, or external heat exchangers. These systems remove heat through cooled surfaces and are most effective when the reactor contents are well circulated. During a thermal excursion, the loss or absence of agitation reduces bulk circulation and may promote thermal stratification and persistent hot regions. Consequently, the liquid near the cooled boundary may cool more rapidly than the vessel core, even when cooling capacity is available [12]-[13]. The stirrerless condition therefore represents a conservative hydrodynamic scenario in which emergency cooling cannot rely on mechanical agitation to redistribute heat. Therefore, an effective cooling strategy must provide both heat removal and internal circulation.

Jet mixing cooling provides a method for combining heat removal with internal circulation. The injected coolant introduces momentum directly into the liquid, forming a shear layer that promotes entrainment and recirculation within the vessel [14]-[15]. Previous studies [16]-[18] have reported that nozzle position, orientation, and flow conditions can strongly influence mixing time and vessel coverage. The jet Reynolds number (Re_j) is also important because it reflects the relative effects of inertial and viscous forces on the injected flow [17]. A higher jet Reynolds number generally strengthens penetration, entrainment, and convective heat transfer. However, stronger jet momentum alone may not

***CORRESPONDING AUTHOR | M.I. Rosli** | ✉ masli@ukm.edu.my
© 2026 The Authors. Published by Universiti Malaysia Pahang Al-Sultan Abdullah Press. This is an open access article under the CC BY-NC 4.0 license

ensure effective vessel-scale cooling if the circulation remains spatially limited. This was reported by [19], who reported that the mixing time is influenced by the jet orientation. These findings indicate that both jet momentum and flow organization are important in determining the mixing performance for thermal stability. However, existing jet mixing studies have characterized the performance predominantly through the overall mixing time for general process mixing [16], [20]. Even within this context, the reported optimum injection angles vary considerably between studies [16]-[18]. Hydrodynamic effects on transient reactor cooling also remain insufficiently characterized, despite their influence on internal circulation and local heat transport [21]. Thermal safety studies commonly focus on reaction kinetics, detection, relief, or chemical inhibition [12], [22]-[23]. In studies involving jet mixing and thermal safety, mechanical agitation is generally retained as the main or supplementary source of circulation rather than relying on jet-induced circulation alone [20], [24]. Consequently, stirrerless jet-cooled configurations have received limited attention. Although jet configurations have been widely investigated for mixing applications, experimental evidence on their influence on transient cooling for thermal runaway mitigation remains limited, particularly in stirrerless vessels.

Experimental measurements capture the transient cooling response only at the sensor locations. They cannot fully reveal the three-dimensional velocity and temperature fields within the vessels. Milewska and Molga [25] also concluded that thermocouple placement can be crucial for detecting early runaway scenarios. This limitation highlights the need for a numerical approach that can resolve the internal hydrodynamic and thermal fields beyond the measurement points. Computational fluid dynamics (CFD) provides a suitable approach for this purpose by resolving jet penetration, recirculation, vortex development, and spatial temperature variations that cannot be fully captured by point temperature measurements alone [14], [16]-[17], [26]. Transient simulations capture the evolution of the flow and temperature fields as the jet develops and cooling progresses. A validated transient CFD model can therefore relate the measured cooling response to the underlying flow structures. To address this, the present study investigated jet Reynolds number-driven cooling enhancement using a combined experimental and CFD framework. Experiments established the transient cooling response and provided data for CFD validation. The validated model was then extended over a wider jet Reynolds number range to examine the corresponding temperature and streamline fields. Cooling performance was evaluated using normalized temperature (θ) and cooling time indicators (t_{50} and t_{90}). The value of t_{50} is defined as the time required for θ to reach 0.5 (50% thermal homogenization) and is associated with the fast-transient cooling phase. In contrast, t_{90} is defined as the time required for θ to reach 0.1 (90% thermal homogenization) and is associated with the asymptotic cooling phase. The study compared a 45° side jet and a 90° axial bottom jet to evaluate the effects of jet orientation and flow intensity on transient cooling. By relating these cooling indicators to the resolved circulation structures, the study examined how jet momentum and hydrodynamic structure influenced transient cooling in a stirrerless reactor. The findings provide design guidance for jet-based emergency cooling and support improved thermal control during reactor thermal excursions.

2. Materials and Methods

2.1 Experimental Setup for Model Validation

Figure 1 shows the experimental jet mixing cooling system. A vertical cylindrical reactor (0.16 m in diameter and 0.74 m in height) was connected to a coolant supply, pump, flowmeters, valves, injection nozzles, drain outlet, and data acquisition system. The vessel was initially filled with hot water. The cooling liquid was then introduced through either a 45° side jet or a 90° axial bottom jet. The flowmeters (F1, F2) measured the volumetric flow rate, while regulating valves (V1, V2) were used to set the required operating conditions. Valve V3 was kept closed throughout the experiment to ensure that the flow was directed only to nozzle 2 (N2). Simultaneous drainage maintained the liquid level during coolant injection.

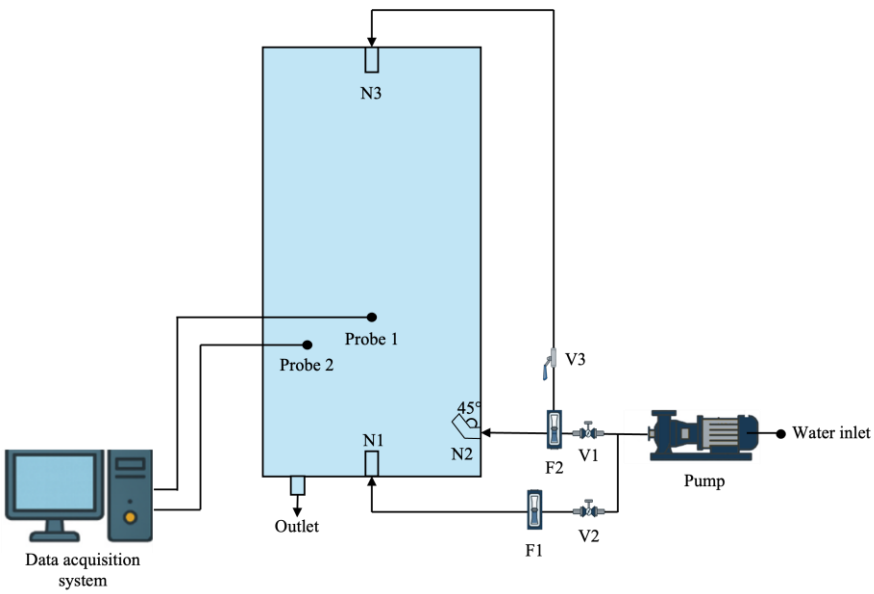

Figure 1. Schematic diagram showing the arrangement of nozzles (N1, N2, N3), thermocouples (Probe 1, 2), flowmeters (F1, F2), valve (V1, V2, V3), pump and data acquisition system

Water was used as both the initial bulk liquid and the injected coolant. The initial bulk and coolant temperature were approximately 355.45 K and 305.25 K, respectively. The liquid height in the vessel was 0.24 m, giving liquid height to vessel diameter ratio (H/D) was 1.5. The coolant entered through a 0.0032 m nozzle and the displaced liquid left through a 0.0064 m drain. Two Type-K thermocouples (TC1 and TC2) recorded the transient temperature response. TC1 was located 0.226 m above the vessel base and 0.08 m from sidewall, while TC2 was located 0.097 m above the base and 0.035 m from the sidewall. The data acquisition system recorded both temperature histories. These dimensions were reproduced in the CFD simulation using 90° axial bottom jet as a representative geometry. The experimental operating conditions were established from the measured coolant volumetric flow rates. Four flow rates of approximately 0.58, 0.65, 0.72 and 0.78 L/min were investigated, corresponding to mean nozzle exit velocities of approximately 1.20, 1.35, 1.49 and 1.62 m/s, respectively. The jet Re_j was defined based on the mean nozzle exit velocity and nozzle diameter as $Re_j = \rho v d/\mu$, where v is the mean nozzle velocity (m/s), d is the nozzle diameter (m), is the fluid density (kg/m^3) and is the fluid viscosity (Pa·s). For consistency between the experimental and CFD cases, the same constant reference water properties adopted in the CFD model were used to evaluate Re_j, with $\rho = 998.2$ kg/m^3 and $\mu = 1.003 \times 10^{-3}$ Pa·s. Based on a nozzle diameter of 0.0032 m, the corresponding Re_j values were 3828, 4290, 4752 and 5148. These Reynolds numbers were used to identify the respective experimental flow conditions throughout the study.

2.2 CFD Approach

ANSYS 2025 R2 software was used to simulate the three-dimensional transient flow and heat transfer within the vessel. A 90° axial bottom jet was used as a representative geometry. The numerical model represented the coolant jet, hot bulk liquid, drain outlet, vessel walls, and free liquid surface. The CFD study covered a jet Reynolds number range of 3828 to 5808. Four experimental Re_j (3828, 4290, 4752, and 5148) were supplemented by two numerical Re_j (5610 and 5808) to extend the parametric range and examine the progressive effects of jet momentum on transient cooling and internal flow development. A pressure-based transient solver was employed, and the turbulence model, governing equations, and numerical schemes are described in Section 2.2.3.

2.2.1 Geometric model and boundary conditions

Figure 2(a) shows the computational geometry, and 2(b) and (c) show the cross-sectional plane arrangement used for post-processing visualization. The computational domain reproduced the experimental vessel dimensions. The cylindrical liquid domain had a height (H) of 0.24 m and a vessel diameter (D) of 0.16 m, which gave a liquid height to vessel diameter ratio (H/D) of 1.5. The other geometric dimensions used in the experiment were retained to evaluate the effect of the jet orientation under a consistent vessel geometry.

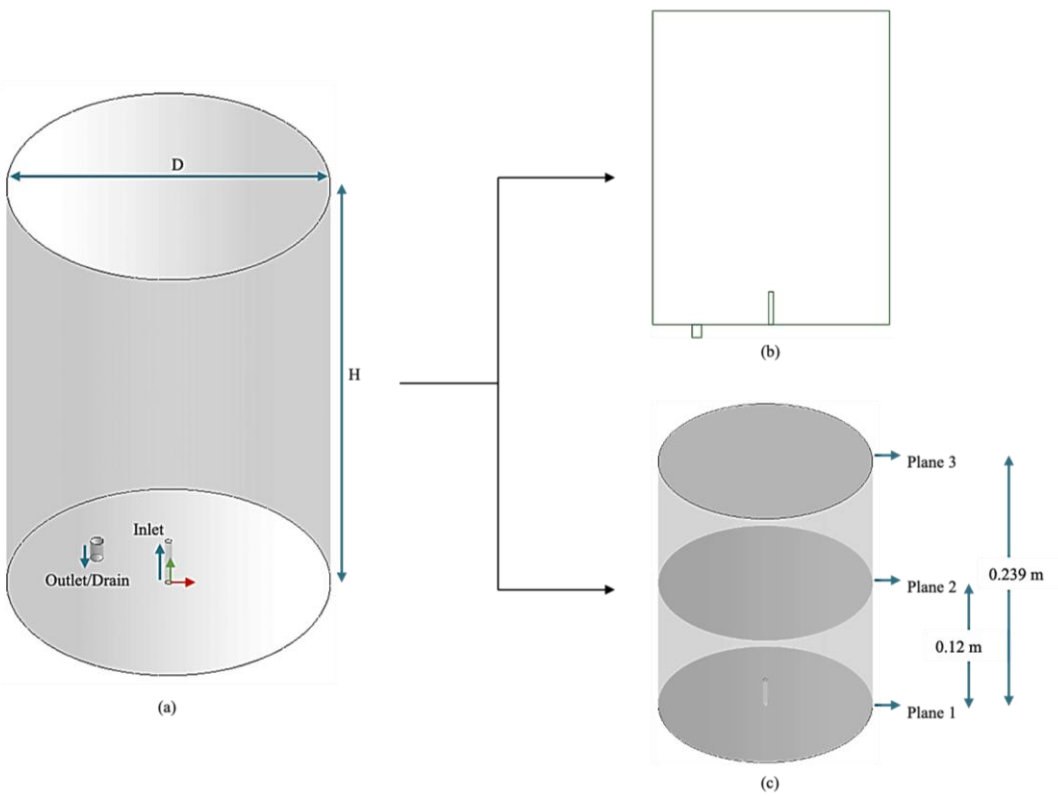

Figure 2. Computational domain geometry of the cylindrical reactor; (a) 3D isometric view showing the fluid domain and nozzle inlet at the base; (b) 2D front cross-sectional view showing the vertical plane used at centre of the reactor for temperature contour and streamline visualisation; (c) Three horizontal cross-sectional planes (Plane 1: bottom, Plane 2: middle, Plane 3: top) used for azimuthal temperature distribution analysis

Table 1 summarizes the boundary conditions applied in the CFD model. The coolant inlet was specified as a velocity inlet, with the velocity calculated from the experimental coolant volumetric flow rates. The outlet was defined as a pressure outlet at zero-gauge pressure, while all solid boundaries were treated as stationary no slip walls. The reactor wall was assumed adiabatic because external heat loss was considered negligible compared with the forced convective cooling generated by the injected jet. This assumption was supported by the close agreement between the experimental and simulated temperature decay. The top liquid surface was represented using a symmetry boundary to approximate a flat liquid-air interface with negligible shear, consistent with previous jet mixing studies [24], [27]. The fluid domain was initialized at a uniform temperature of approximately 355.45 K and zero velocity at the start of each simulation. For CFD simulation, constant water properties in Fluent were used: $\rho = 998.2$ kg/m^3, $\mu = 1.003 \times 10^{-3}$ Pa·s, $C_p = 4182$ J/kg·K, and thermal conductivity = 0.6 W/m·K. The experimental coolant volumetric flow rates were imposed at the velocity inlet. This maintained consistency in nozzle geometry and inlet flow conditions between the experimental and CFD model.

Table 1. Overview of simulation settings and boundary conditions

Boundary or condition	Specification
Fluid domain	Water; constant water properties: $\rho = 998.2$ kg m^{-3}; $\mu = 1.003 \times 10^{-3}$ Pa·s; $C_p = 4182$ J/kg; $\lambda = 0.6$ W/m·K
Coolant inlet	Velocity inlet calculated from the volumetric flow rate; coolant temperature = 305.25 K
Outlet drain	Pressure outlet; gauge pressure = 0 Pa
Reactor walls	Adiabatic, no slip wall
Top surface of the liquid	Symmetry boundary
Initial liquid condition	Uniform temperature = 355.45 K; zero initial velocity
Turbulence specification at inlet	Turbulence intensity = 5%; turbulent viscosity ratio = 10

2.2.3 Governing equation and numerical method

A pressure-based transient solver was employed with the SIMPLE algorithm for pressure–velocity coupling. The gradients were evaluated using the least squares cell-based method. Second-order upwind discretization was applied to the momentum and energy equations, while second-order discretization was used for pressure and first-order upwind for the k and ε equations. Hybrid initialization and double-precision calculations were used. The transient simulations employed a first-order implicit formulation with a time step of 1 s and a maximum of 20 iterations per time step. Each simulation was run for 1800 s because all configurations reached the t_{90} threshold within this period. The convergence criteria were 10^{-6} for energy and 10^{-3} for the remaining equations. The complete solver settings are summarized in Table 2.

Table 2. Summary of simulation features of CFD simulations

Parameter	Conditions/Values
Flow formulation	Single phase, incompressible, transient
Turbulence model	Standard k–ε
Near wall treatment	Enhanced wall treatment
Solver	Pressure based transient solver
Pressure velocity coupling scheme	SIMPLE
Gradient evaluation	Least squares cell based
Spatial discretisation	Second order upwind for momentum and energy; second order for pressure; first order upwind for k and ε
Time step and iterations	1 s; 20 iterations per time step
Residual criterion	10^{-3} for continuity, momentum, k and ε; 10^{-6} for energy
Initialisation	Hybrid initialisation

The CFD model solved the unsteady continuity, Navier–Stokes momentum, and energy equations, along with the standard k–ε turbulence model. The transient terms were retained to resolve the evolution of velocity, pressure, turbulence, and temperature throughout the cooling process. The standard k–ε model was selected because of its established robustness for turbulent jet flow simulations and its balance between computational cost and predictive accuracy over the investigated Reynolds number range of 3828–5808 [19], [24], [28].

The governing equations used in this study are the unsteady, reduced forms of the general transport equations implemented in ANSYS Fluent [29]. The local time derivative terms were retained, while momentum diffusion was represented using the combined molecular and turbulent viscosities. The working fluid was treated as incompressible, single-phase, non-reactive, and constant density. Gravity and hydrostatic effects were incorporated through the pressure field, whereas kinetic energy, pressure work, viscous dissipation, and reaction heat generation were neglected in the energy formulation. For the standard k–ε model, the effect of buoyancy was neglected under the non-buoyant assumption, effect of compressibility on turbulence was omitted for incompressible flow, and no additional source terms were imposed. Reynolds stresses were closed using the Boussinesq eddy viscosity hypothesis. The reduced governing equations are presented in Eqs. (1-7).

(1) The continuity equation, representing the conservation of mass for this incompressible, constant-density flow, is given by Eq. (1).

$$\frac{\partial u_i}{\partial x_i} = 0 \tag{1}$$

where u_i is the velocity component in direction i, and x_i is the corresponding spatial coordinate.

(2) The momentum equation is expressed as Eq. (2).

$$\frac{\partial(\rho u_i)}{\partial t} + \rho u_j \frac{\partial \mathrm{u_i}}{\partial \mathrm{x_j}} = -\frac{\partial p}{\partial \mathrm{x_i}} + \frac{\partial}{\partial x_j}\left[\mu\left(\frac{\partial u_i}{\partial x_j} + \frac{\partial u_j}{\partial x_i}\right) - \rho u_i u_j\right] \tag{2}$$

The Reynolds stress term in Eq. (2) is closed using the Boussinesq eddy viscosity hypothesis, as shown in Eq. (3).

$$\rho u_i u_j = \mu_t\left(\frac{\partial u_i}{\partial x_j} + \frac{\partial u_j}{\partial x_i}\right) - \frac{2}{3}\delta_{ij}\rho k \tag{3}$$

In this equation, u_i and u_j denote the velocity components in the i and j directions, x_i and x_j represent the corresponding spatial coordinates, ρ is fluid density, p is pressure, μ and μ_t are the molecular and turbulent dynamic viscosities, δ_{ij} is the Kronecker delta, k is turbulent kinetic energy and t is time.

(3) The energy equation is expressed as Eq. (4).

$$\frac{\partial(\rho T)}{\partial t} + \rho \mathrm{u_j} \frac{\partial T}{\partial x_j} = \frac{\partial}{\partial \mathrm{x_j}}\left[\left(\frac{\mu}{\sigma} + \frac{\mu_t}{\sigma_t}\right)\frac{\partial \mathrm{T}}{\partial \mathrm{x_j}}\right] \tag{4}$$

where T is temperature, σ and σ_t are the molecular and turbulent Prandtl number, respectively.

(4) The transport equation for turbulent kinetic energy, k, is given by Eq. (5).

$$\frac{\partial(\rho k)}{\partial t} + \rho u_j \frac{\partial k}{\partial x_j} = \frac{\partial}{\partial x_j}\left[\left(\mu + \frac{\mu_t}{\sigma_k}\right)\frac{\partial k}{\partial x_j}\right] + \mu_t\left(\frac{\partial u_i}{\partial x_j} + \frac{\partial u_j}{\partial x_i}\right)\frac{\partial u_j}{\partial x_i} - \rho\varepsilon \tag{5}$$

where σ_k is turbulent Prandtl number for k and ε is turbulent dissipation rate.

(5) The transport equation for the turbulent dissipation rate, ε, is given by Eq. (6).

$$\frac{\partial(\rho\varepsilon)}{\partial t} + \rho u_j \frac{\partial \varepsilon}{\partial x_j} = \frac{\partial}{\partial x_j}\left[\left(\mu + \frac{\mu_t}{\sigma_\varepsilon}\right)\frac{\partial \varepsilon}{\partial x_j}\right] + C_{1\varepsilon}\frac{\varepsilon}{k}\mu_t\left(\frac{\partial u_i}{\partial x_j} + \frac{\partial u_j}{\partial x_i}\right)\frac{\partial u_j}{\partial x_i} - C_{2\varepsilon}\rho\frac{\varepsilon^2}{k} \tag{6}$$

where

$$\mu_t = \rho C_\mu \frac{k^2}{\varepsilon} \tag{7}$$

In this equation, σ_ε is turbulent Prandtl number for ε and $C_{1\varepsilon}$, $C_{2\varepsilon}$ and C_μ are the constant. The standard k–ε closure coefficients were $C_{1\varepsilon} = 1.44$, $C_{2\varepsilon} = 1.92$, $C_\mu = 0.09$, $\sigma_k = 1.0$ and $\sigma_\varepsilon = 1.3$.

2.2.4 CFD model verification and validation

Prior to the parametric CFD study, numerical verification and validation were performed to establish the credibility of the CFD model. Mesh independence was first assessed to determine the influence of grid resolution on the predicted flow and thermal fields. An unstructured tetrahedral mesh was used because of its flexibility in representing the cylindrical vessel and different nozzle orientations, consistent with the approach reported by Li et al. [30]. Four mesh densities were evaluated using the volume average velocity as a monitoring parameter. In addition to mesh independence, the mesh quality was evaluated using skewness and orthogonal metrics. For skewness, lower values indicate a better element quality. Values below 0.94 are generally considered acceptable, whereas values approaching 1.0 indicate poor or unacceptable mesh quality. For orthogonal quality, higher values indicate a better mesh quality. Values above 0.15 are generally considered acceptable, whereas values approaching 1.0 represent excellent element quality [31].

The second procedure involved the validation of the CFD model against experimental thermocouple measurements. Both the mesh independence study and model validation were performed using a 90° axial bottom jet at a jet Reynolds number of 3828 to maintain consistent geometrical and operating conditions. Once the mesh configuration and numerical settings were verified and the CFD model was validated, the same modelling framework was applied to the remaining jet configurations and operating conditions in the parametric study.

2.3 Cooling Performance Indicators and Hydrodynamic Analysis

To quantitatively evaluate the effectiveness of the cooling process, the temperature evolution within the vessel was analyzed using a normalized temperature parameter (θ) [30]-[32]. The normalized temperature is defined as Eq. (8).

$$\theta = \frac{T - T_{cool}}{T_{initial} - T_{cool}} \tag{8}$$

where T represents the instantaneous temperature, $T_{initial}$ is the initial reactor temperature, and T_{cool} is the temperature of the injected cooling jet. Normalization enables the transient cooling behavior to be compared across different jet configurations and operating conditions by eliminating the impact of absolute temperature values. Let the normalized temperature decrease from θ = 1 (initial condition) toward values approaching zero as thermal equilibrium is approached.

To measure the transient cooling performance, two characteristic cooling indicators were isolated by extracting them from the normalized temperature curves. The first indicator, t_{50}, is the time taken for the vessel to achieve 50% thermal homogenization, which is equivalent to θ = 0.5. The second indicator, t_{90}, is the time taken to reach 90% thermal homogenization, which is equivalent to θ = 0.1. These parameters are useful measurements of cooling efficiency, with t_{50} reflecting the early-to-intermediate cooling behavior and t_{90} indicating the final mixing and homogenization phase of the cooling process [20], [33]. In addition, the cooling process was analyzed using velocity contours and streamline patterns to identify recirculation zones, vortex structures, and overall flow distribution. The transient cooling response was divided into three phases for hydrodynamic interpretation: the initial phase (associated with jet development and localized cooling near the inlet), the fast transient phase (associated with developed recirculation and convective heat transport), and the asymptotic phase (associated with later approach toward thermal homogenization). This analysis was used to relate the resolved flow structures to the cooling indicators and assess the effects of jet Reynolds number and configuration on transient cooling behavior. In addition, the relative cooling improvement was calculated by comparing the cooling time of each selected jet configuration with a baseline jet configuration. The percentage cooling time improvement was determined using Eq. (9).

$$(\%) = \left|\frac{(t_{baseline} - \mathrm{t})}{t_{baseline}}\right| \times 100 \tag{9}$$

where $t_{baseline}$ represents the cooling time of the baseline configuration, and t represents the cooling time of the selected configuration at the same cooling threshold. This expression is applicable to all the investigated jet configurations. To ensure consistency, the comparison must be performed using the same cooling indicator, such as t_{50} and t_{90}. A positive improvement value indicates that the selected configuration reaches the specified cooling threshold faster than the baseline.

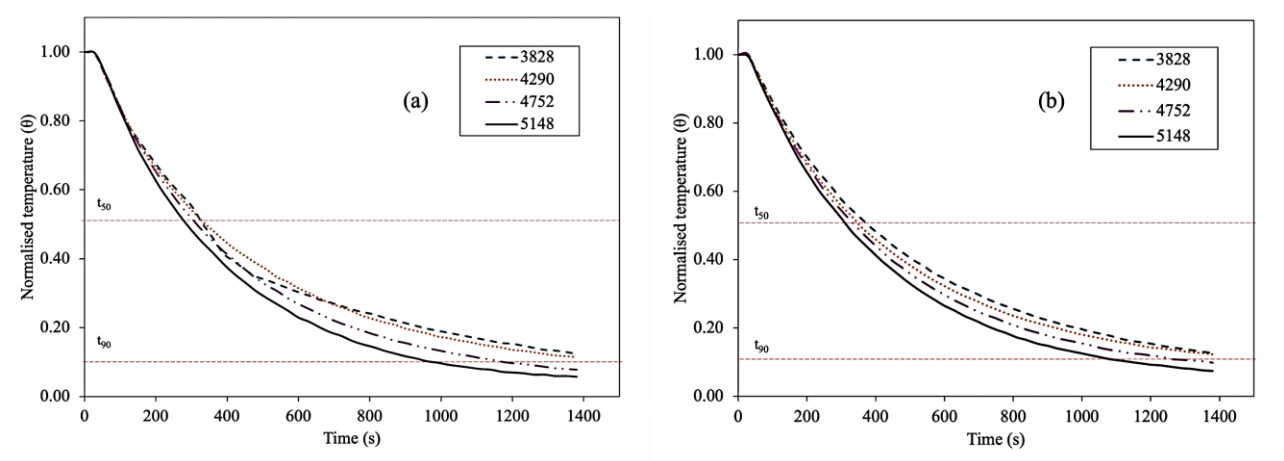

Figure 3. Experimental normalised temperature profiles for (a) the 90° axial bottom jet and (b) the 45° side jet, Re_j = 3828 to 5148

3. Results and Discussion

3.1 Experimental Transient Cooling Response

Figure 3 shows the experimental normalized temperature profile of the 90° axial bottom jet and 45° side jet for the four jet Re_j. In both jet configurations, θ decreases continuously with time. The curves also progressively separate as the jet Reynolds number increases. This indicates that increasing the jet Reynolds number accelerates cooling by enhancing jet penetration, entrainment, and vessel circulation. As a result, a higher jet Reynolds number produces lower θ values, with Re_j = 5148 achieving the lowest final normalized temperature in both configurations. However, both jet configurations show different cooling behaviors, particularly between t_{50} and t_{90}. The temperature profiles separate more widely as the jet Reynolds number increases for the 90° axial bottom jet. The 45° side jet also shows faster cooling at higher Reynolds numbers, but the curves remain closer together, particularly at lower Reynolds numbers. This indicates that increasing the coolant volumetric flow rate improves cooling in both configurations, but the improvement is more effective for the axial bottom jet. This cooling behavior observation is consistent with previous jet mixing studies. Patwardhan [34] demonstrated that jet-mixed vessels are strongly affected by local flow structures, causing the temperature or concentration profile to vary with measurement location. Similarly, Oluwadero et al. [18] observed that nozzle position

strongly affects mixing efficiency in large vessels. Therefore, the present results indicate that increasing the jet Reynolds number enhances transient cooling, but the overall cooling performance is also strongly governed by jet orientation and the circulation pattern generated inside the vessel. Overall, the results indicate that jet mixing has the potential to serve as an emergency cooling strategy for non-stirred reactors, particularly for enhancing heat removal during transient thermal events. Among the tested configurations, the 90° axial bottom jet provides stronger transient cooling than the 45° side jet, as shown by its shorter cooling time and lower final θ values across the jet Reynolds number range. This behavior is further investigated through CFD analysis, where the hydrodynamic flow field and temperature distribution are examined to clarify how jet mixing enhances heat removal, improves thermal stability, and supports thermal runaway mitigation.

3.2 Model Verification and Validation

Figure 4(a) shows the computational mesh, including the local refinement applied around the jet inlet to resolve the steep velocity and temperature gradients in this region. Figure 4(b) presents the mesh independence assessment, based on the volume average velocity in the vessel for four mesh densities of approximately 137790, 209410, 298850, and 534780 elements. To verify that the results of the simulation do not depend on the grid size, a mesh independence test must be performed with various mesh densities [35], [36]. The effect of the velocity changes insignificantly beyond approximately 298850 elements, which implies mesh-independent behavior. Thus, the mesh containing approximately 298850 elements was chosen in all further simulations, and it provides a good compromise between computation speed and accuracy of solutions.

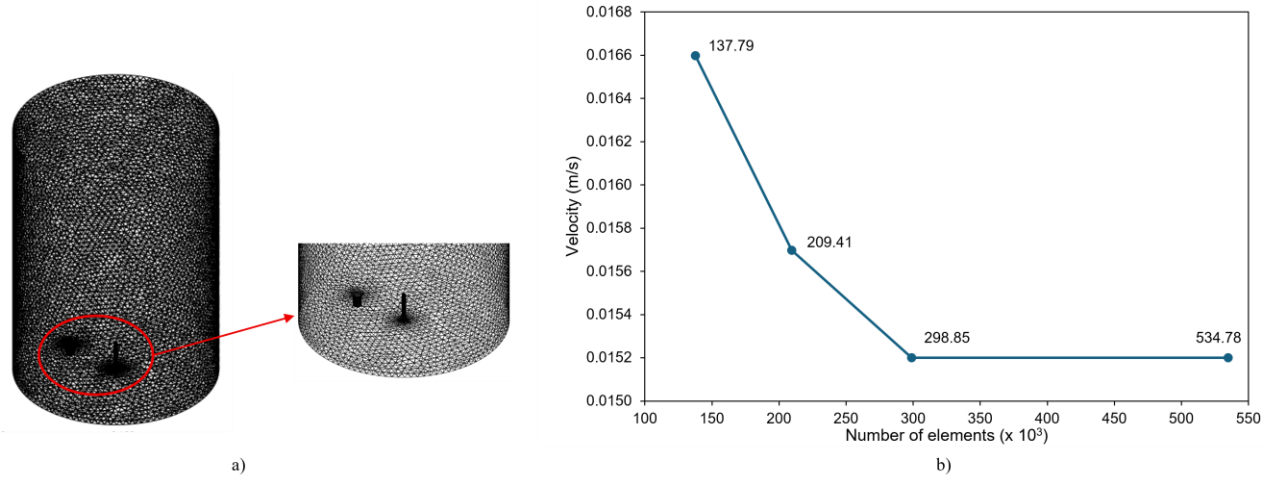

Figure 4. (a) Computational mesh and local inlet refinement and (b) mesh independence assessment of the model

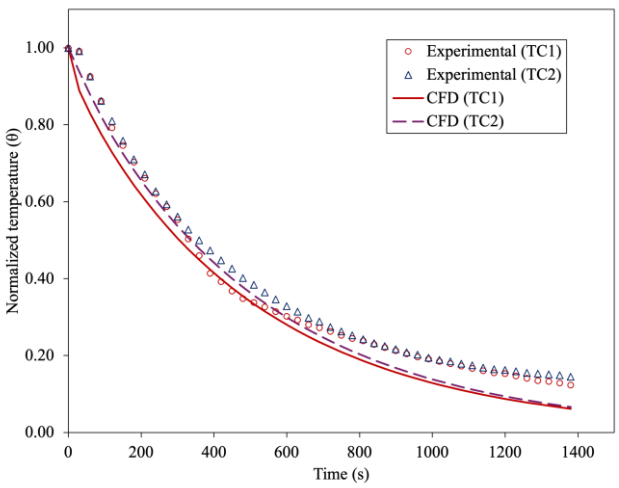

Figure 5. CFD model validation for the 90° axial bottom jet at TC1 and TC2

The transient CFD prediction was then compared with the experimental measurements for the 90° axial bottom jet at both thermocouple locations, as shown in Figure 5. The results compare the CFD and experimental normalized temperature responses for the 90° axial bottom jet at TC1 and TC2. Both measured profiles showed continuous decay during the cooling period, and the numerical curves followed the same experimental transient shape. The close correspondence across the validation period indicates that the model reproduces the measured cooling trends at both spatial locations. The quantitative agreement is summarized in Table 3. Based on 47 sampled times over the 0–1380 s validation period, the mean relative errors were 0.91% and 0.88% at TC1 and TC2, respectively, whereas the corresponding maximum errors were 1.94% and 1.31%, respectively. The agreement at two spatially separated locations

indicates that the model reproduces the dominant transient thermal response of representative axial geometry. The validation does not imply that every local velocity feature is exact; however, it provides a credible basis for applying the same numerical framework to subsequent jet Reynolds number and configuration comparison.

Table 3. Summary of CFD model validation for the 90° axial bottom jet

Probe	Validation points	Mean error (%)	Maximum error (%)
TC1	47	0.91	1.94
TC2	47	0.88	1.31

3.3 Influence of Jet Reynolds number on Transient Cooling Behaviour

Figure 6 shows the CFD-normalized temperature curves for the 90° axial bottom jet and 45° side jet at Re_j = 3828–5808. For both configurations, the cooling curves exhibited a clear exponential decay pattern, which was consistent with the experimental temperature profile. The temperature decreases rapidly during the initial and intermediate transient stages ($\theta = 0 – 0.15$), followed by a gradual approach toward thermal equilibrium during the later stage ($\theta < 0.15$). This behavior is typical of jet-induced convective cooling, where the early cooling stage is dominated by jet penetration and bulk entrainment, whereas the late stage is controlled by residual thermal homogenization. Increasing the jet Reynolds number consistently accelerated the temperature decay for both jet configurations. At higher Reynolds numbers, the curves shifted downward and reached the t_{50} and t_{90} thresholds earlier. This indicates that increasing the jet momentum enhances the convective transport, strengthens the entrainment of the surrounding hot fluid, and promotes a faster thermal exchange between the coolant and vessel bulk. This improvement was not limited to the early cooling periods. The higher Reynolds number configuration also maintained lower normalized temperature values during the asymptotic phase, indicating that stronger turbulence improved both rapid cooling and final homogenization.

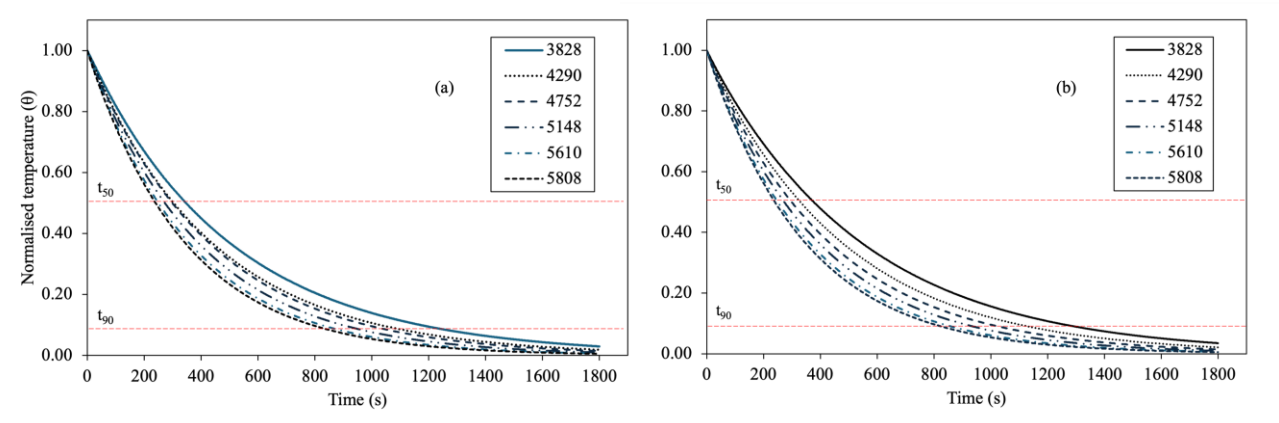

Figure 6. CFD normalised temperature profiles for (a) the 90° axial bottom jet and (b) the 45° side jet, Re_j = 3828 to 5808

Figure 7 shows the temperature contours for the two jet configurations at Re_j = 3828. At 1 s, both vessels remained close to the initial thermal conditions, and the cooled region was concentrated near the inlets. At 10 s, the cooling effect was influenced by the jet penetration, with the 90° axial bottom jet exhibiting a longer length than the 45° side jet. By 200 s, the cooling effect had spread over a larger volume of the substrate. The axial bottom jet produced a more vertically distributed temperature field, whereas the side jet exhibited a stronger lateral bias towards the injection side. At 1000 and 1500 s, both configurations approached a more uniform low-temperature state; however, the axial configuration remained slightly cooler than the radial configuration. The difference in the thermal fields between the two jet configurations was small during the first few seconds because the injected coolant initially affected only a limited area. As circulation developed, the thermal fields began to diverge. The axial jet directs the momentum through the vessel core and establishes a more direct vertical circulation pathway than the radial jet. In contrast, the side jet interacted with the wall and redistributed the coolant through an asymmetric loop. Therefore, different cooling responses emerged from the sustained circulation field rather than from the initial coolant entries. This difference in momentum distribution explains why the side jet cools the monitored region more slowly [18]. This finding provides an important link between the temperature curves and the hydrodynamic analysis. At the same jet Reynolds number, both configurations exhibited comparable flow intensities but developed different spatial temperature distributions. This indicates that jet orientation influences the conversion of the supplied momentum into vessel-scale thermal transport. Overall, the jet Reynolds number determines the intensity of convective cooling, whereas the jet orientation determines the effectiveness of the transport distribution in the vessel.

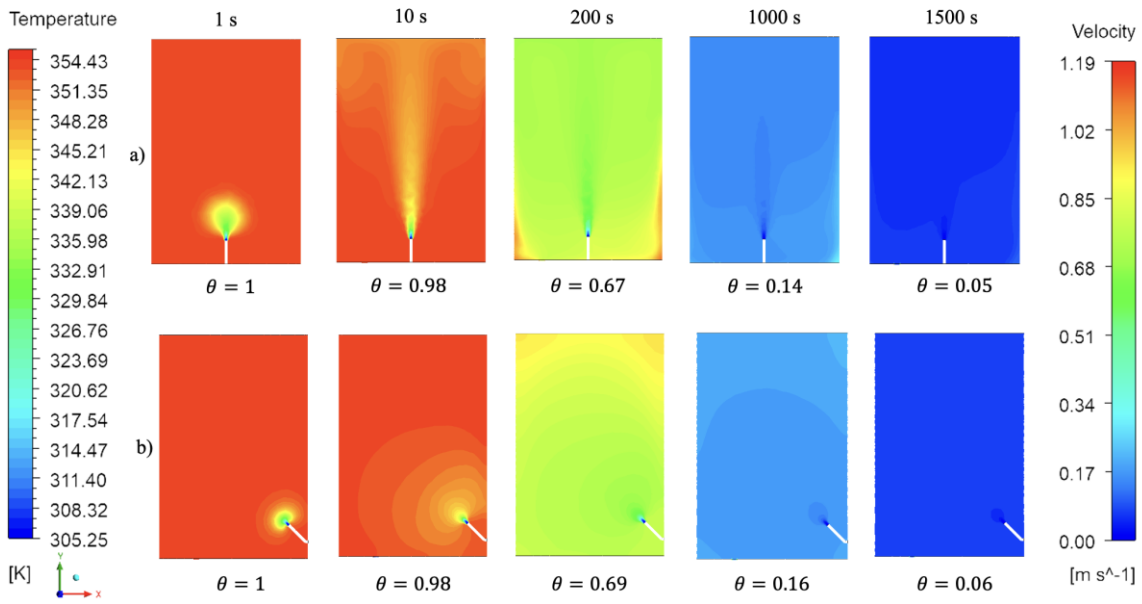

Figure 7. Temperature contours at selected times for (a) the 90° axial bottom jet and (b) the 45° side jet at Re_j = 3828

3.4 Axial Jet Temperature Field and Hydrodynamic Mechanism

Figure 8(a) shows the temperature contours and corresponding streamline patterns for the 90° axial bottom jet at representative jet Reynolds numbers. The results indicate that an increase in the jet Reynolds number accelerated the cooling process and strengthened the associated recirculation structure. At 10 s, all temperature contours remained close to the initial thermal condition (θ = 0.97–0.98), indicating that the cooling effect remained localized near the jet inlet. By 200 s, the effect of the jet Reynolds number became clearer, with θ decreasing from approximately 0.67 at Re_j = 3828 to 0.54 at Re_j = 5808. At 1000 s, the θ values decreased further from approximately 0.14 to 0.05, indicating that a higher Re_j improved both the intermediate and later stages of the cooling process.

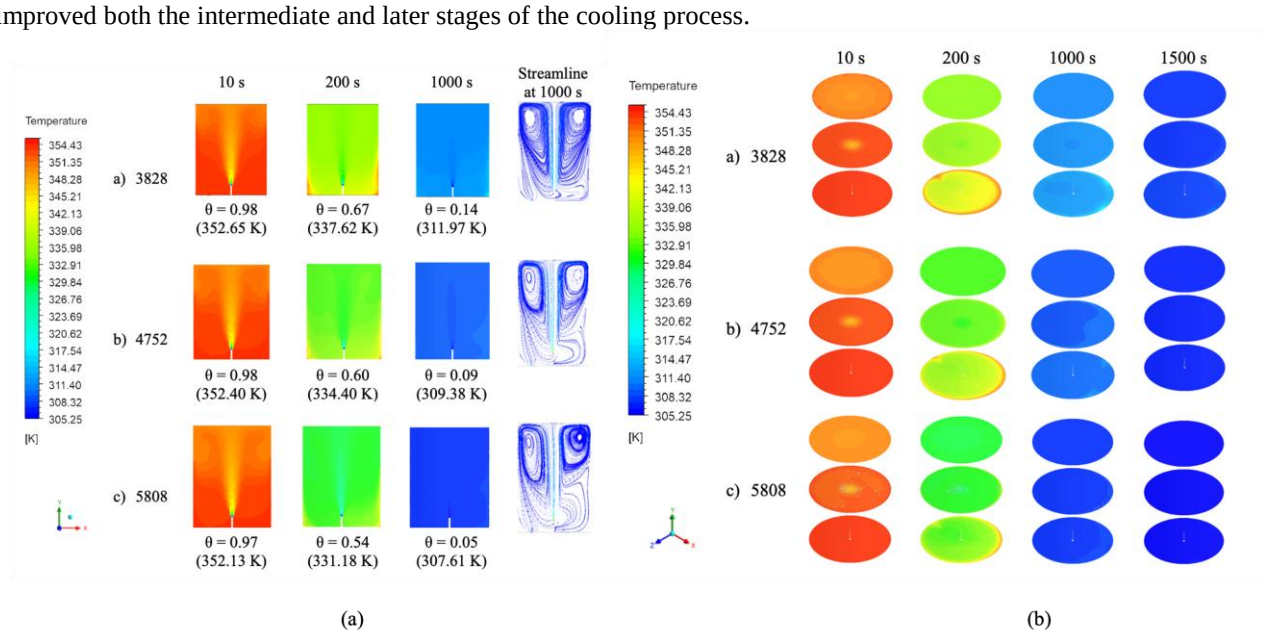

Figure 8. (a) Temperature contours and streamlines for the 90° axial bottom jet at representative Reynolds numbers; (b) Top view temperature contours at selected times and vessel elevations

The streamline patterns explain this thermal response. The axial jet generates a pair of counter-rotating recirculation cells around the vertical jet axis, directing the fluid upward through the vessel core and returning it downward near the wall. This circulation promotes fluid redistribution throughout the vessel and limits the weakly mixed regions. As Re_j increases, the recirculation becomes stronger, enhancing momentum transfer and convective heat transport. The observed counter-rotating vortex structure and its role in distributing jet momentum are consistent with the hydrodynamic mechanisms reported for jet-driven mixing in cylindrical vessels [14]-[15]. In addition, Figure 8(b) presents the corresponding top-view temperature contours at selected times and vessel elevations. At 10 s, most of the vessel remains hot, with cooling concentrated near the jet core. By 200 s, the cooled region extends through the bottom (plane 1) and middle (plane 2) sections of the vessel. At 1000 s and 1500 s, the temperature field becomes progressively more uniform across the vessel height, particularly at higher jet Reynolds numbers.

3.5 Side Jet Temperature Field and Hydrodynamic Mechanism

Figure 9(a) presents the temperature contours and corresponding streamline patterns for the 45° side jet at representative jet Reynolds numbers. The results show that the 45° side jet also exhibits faster cooling as the jet Reynolds number increases. At 200 s, θ decreases from 0.69 at Re_j = 3828 to 0.56 at Re_j = 5808. By 1000 s, the θ values decrease further from approximately 0.16 to 0.05. However, the streamline patterns reveal a more asymmetric circulation structure than that of the axial jet. In addition, Figure 9(b) presents the corresponding top-view temperature contours at selected times and vessel elevations. The temperature contours provide additional evidence of the asymmetric cooling behavior of the side jet. At 10 s, the cooling zone is concentrated near the injection region. The asymmetry remains visible at 200 s, particularly in the bottom (plane 1) and middle (plane 2) sections. Although the temperature fields become more uniform at 1000 s and 1500 s, the side jet continues to show greater lateral temperature variation compared with the axial jet.

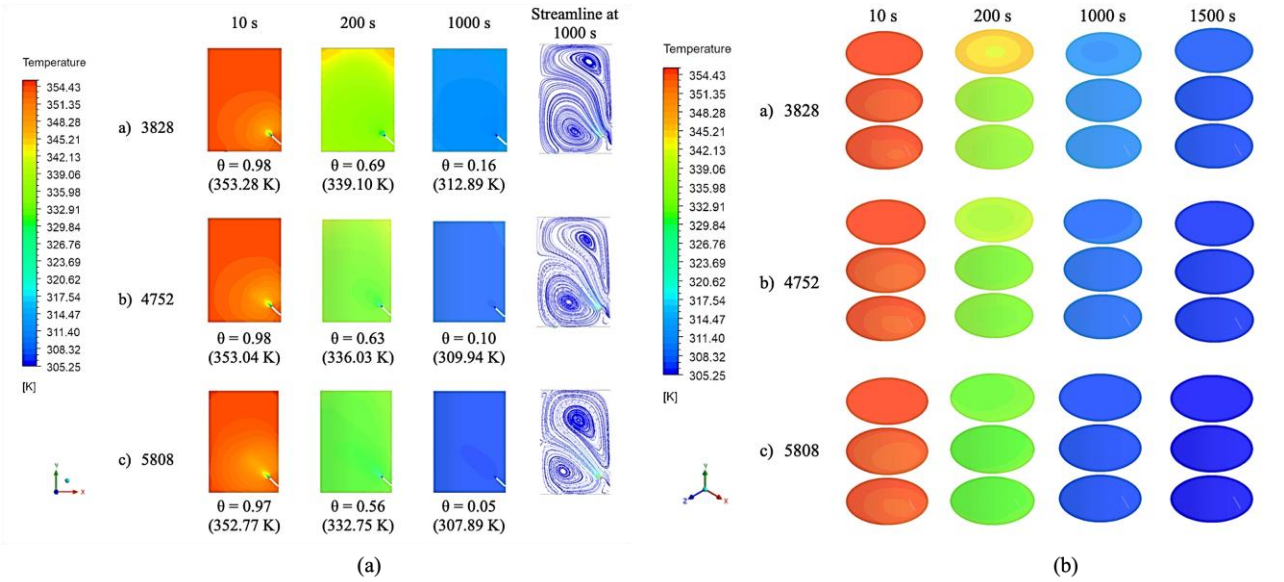

Figure 9. (a) Temperature contours and streamlines for the 45° side jet at representative Reynolds numbers; (b) Top view temperature contours at selected times and vessel elevations

Table 4. Summary of t_{50}, t_{90}, cooling time improvement for the 90° axial bottom jet and 45° side jet configurations

Jet Reynolds number (Re_j)	Jet configuration	t_{50} (s)	t_{90} (s)	Cooling time improvement at t_{50}	Cooling time improvement at t_{90}
3828	45° side jet	372	1212	Baseline	Baseline
4290		325	1060	12.6%	12.5%
4752		295	961	20.7%	20.7%
5148		269	878	27.7%	27.6%
5610		247	805	33.6%	33.6%
5808		237	773	36.3%	36.2%
3828	90° axial bottom jet	342	1145	Baseline	Baseline
4290		300	1008	12.3%	12.0%
4752		272	915	20.5%	20.1%
5148		248	838	27.5%	26.8%
5610		229	773	33.0%	32.5%
5808		220	744	35.7%	35.0%

3.6 Cooling Performance Indicators and Reactor Safety Implications

Table 4 summarizes the t50, t90, and cooling time improvements of both jet configurations at representative jet Reynolds numbers. For the 45° side jet, t_{50} decreases from 372 s to 237 s, with a reduction of 36.3%. Its t_{90} decreases from 1212 s to 773 s, with a reduction of 36.2%. For the 90° axial bottom jet, t_{50} decreases from 342 s at Re_j = 3828 to 220 s at Re_j = 5808, while t_{90} decreases from 1145 s to 744 s. These reductions correspond to 35.7% and 35.0%, respectively. These reductions indicate that the jet Reynolds number is a dominant operating parameter controlling the transient cooling performance. Table 5 shows the percentage of time reduction between the 90° axial bottom and 45° side jet configurations. The axial jet consistently provides shorter cooling times across all jet Reynolds numbers. Relative to the 45° side jet, the 90° axial bottom jet reduces t_{50} by 8.1% at Re_j = 3828, 7.8% at Rej = 4752, and 7.2% at Re_j = 5808. The corresponding reductions in t_{90} are 5.5%, 4.8%, and 3.8%, respectively. Overall, the improvement ranges from 3.8% to 8.1%, with a

greater reduction observed for t_{50}. The reduction in t_{50} is particularly important because it represents a faster temperature decrease during the earlier phase of thermal excursion. The reduction in t_{90} indicates a shorter time to approach thermal stabilization. Together, these indicators describe the cooling performance during both the earlier and later phases of the transient response. The axial jet provides lower values of both indicators, indicating faster overall cooling than the side jet.

The quantitative improvements observed for the axial jet are also relevant from a reactor safety perspective. These reductions can shorten the duration of high-temperature conditions during a thermal excursion and reduce localized hot regions. The importance of hydrodynamic effects in assessing cooling performance was also highlighted by Kummer and Varga [21]. They noted that thermal runaway studies often neglect system-specific flow patterns, even though internal circulation and local heat transport can significantly influence runaway development and the formation of temperature hot spots. Overall, these results show that the cooling performance depends not only on the flow intensity but also on the distribution of the injected momentum within the vessel. Therefore, the jet configuration should be considered together with the jet Reynolds number when designing cooling systems for reactor thermal stability.

Table 5. Percentage of time reduction between 90° axial bottom jet and 45° side jet configurations

Jet Reynolds number (Re_j)	Indicator	45° side jet	90° axial bottom jet	Time reduction percentage (90° vs 45° jet)
3828	t_{50}	372 s	342 s	8.1%
	t_{90}	1212 s	1145 s	5.5%
4752	t_{50}	295 s	272 s	7.8%
	t_{90}	961 s	915 s	4.8%
5808	t_{50}	237 s	220 s	7.2%
	t_{90}	773 s	744 s	3.8%

4. Conclusions

This study systematically investigated the effects of the jet Reynolds number and jet configuration on the transient cooling performance and hydrodynamic characteristics using a validated CFD model. Increasing the jet Reynolds number from 3828 to 5808 reduced the cooling times by approximately 35–36% for both configurations, demonstrating the strong influence of flow intensity on transient cooling. The 90° axial bottom jet consistently outperformed the 45° side jet, providing an additional 3.8% to 8.1% reduction in cooling time across the investigated jet Reynolds number range. The improved performance of the axial configuration was associated with a more effective circulation structure and better distribution of the injected momentum throughout the vessel. Overall, the findings show that transient cooling performance depends on both jet Reynolds number and jet configuration. Higher Rej strengthens convective transport, while jet configuration determines how effectively this transport is distributed within the vessel. From a reactor cooling perspective, the shorter t_{50} and t_{90} values obtained with the axial bottom jet indicate faster temperature reduction and a shorter time to approach thermal homogenization. These findings highlight the importance of considering both flow intensity and hydrodynamic structure when designing jet mixing cooling systems for stirrerless reactors during thermal excursions.

Acknowledgements

The authors would like to acknowledge the support of Universiti Teknologi MARA, Shah Alam, Selangor, Malaysia, and Faculty of Engineering and Built Environment, Universiti Kebangsaan Malaysia, Bangi, Selangor for providing the facilities for this research.

Funding

This study was not supported by any grants from funding bodies in the public, private, or not-for-profit sectors.

Declaration of Competing Interests

The authors declare no conflict of interest.

CRediT Author Contribution Statement

Nadia Kamarrudin: Conceptualization, methodology, investigation, validation, formal analysis, writing – original draft.
Masli Irwan Rosli: Conceptualisation; Software; Supervision; Writing – review & editing
Mohd Sobri Takriff: Conceptualization, Analysis, Supervision, Writing – review & editing;

Availability of Data and Materials

The datasets generated and/or analyzed during the current study are available from the corresponding author upon reasonable request.

Ethics Statement

This study did not involve human participants or animal subjects. Therefore, ethical approval was not required for this study.

Generative Artificial Intelligence Disclosure

Artificial intelligence tools [ChatGPT Plus] were used to assist with literature summarization, language refinement, and readability. All AI-generated content was reviewed and verified by the authors for accuracy and originality. The final interpretations and conclusions are the sole responsibility of the authors.

References

[1] A. Kummer, T. Varga, and J. Abonyi, "Genetic programming-based development of thermal runaway criteria," *Computer Chemical Engineering*, vol. 131, p. 106582, 2019, https://doi.org/10.1016/j.compchemeng.2019.106582.

[2] C. Villemur, L. Petit, N. Bianchini, and P. Rotureau, "Runaway reaction hazard assessment for chemical processes safety," *Chemical Engineering Transactions*, vol. 77, pp. 451–456, 2019, https://doi.org/10.3303/CET1977076.

[3] S. G. Balasubramanian and J. F. Louvar, "Study of major accidents and lessons learned," *Process Safety Progress*, vol. 21, no. 3, pp. 237–244, 2002, https://doi.org/10.1002/prs.680210309.

[4] A. Dakkoune, L. Vernières-Hassimi, S. Leveneur, D. Lefebvre, and L. Estel, "Risk analysis of French chemical industry," *Safety* Science, vol. 105, pp. 77-85, 2018, https://doi.org/10.1016/j.ssci.2018.02.003.

[5] V. V. Londhe and K. S. Deshmukh, "Practical approach to prediction and prevention of runaway reactions," *World Journal of Advanced Research and Reviews*, vol. 16, no. 2, pp. 139–144, 2022, https://doi.org/10.30574/wjarr.2022.16.2.1137.

[6] T. Abbasi, H. J. Pasman, and S. A. Abbasi, "A scheme for the classification of explosions in the chemical process industry," *Journal of Hazardous Materials*, vol. 174, no. 1–3, pp. 270–280, 2010, https://doi.org/10.1016/j.jhazmat.2009.09.047.

[7] Y. N. Yang, J. Jin, L. T. Zhu, Y. N. Zhou, and Z. H. Luo, "Runaway criteria for predicting the thermal behavior of chemical reactors," *Current Opinion in Chemical Engineering*, vol. 43, p. 100986, 2024, https://doi.org/10.1016/j.coche.2023.100986.

[8] Q. Chen, L. Ni, J. Jiang, and Q. Wang, "Modeling of runaway inhibition in batch reactors using encapsulated phase change materials," *Renewable Energy*, vol. 170, pp. 387–399, 2021, https://doi.org/10.1016/j.renene.2021.01.132.

[9] Y. Wu, H. Ye, and H. Dong, "An inherently safer design approach based on process safety time for batch chemical reaction processes," *Process Safety and Environmental Protection*, vol. 171, pp. 353–364, 2023, https://doi.org/10.1016/j.psep.2023.01.007.

[10] J. Jiang, J. Yang, J. Jiang, Y. Pan, Y. Yu, and D. Zhou, "Numerical simulation of thermal runaway and inhibition process on the thermal polymerization of styrene," *Journal of Loss Prevention in the Process Industries*, vol. 44, pp. 465–473, 2016, https://doi.org/10.1016/j.jlp.2016.10.017.

[11] Y. Wu, H. Ye, and H. guang Dong, "A Multi-objective optimization for batch chemical reaction Processes: The trade-off between economy and safety," *Chemical Engineering Science*, vol. 265, p. 118231, 2023, https://doi.org/10.1016/j.ces.2022.118231.

[12] J. Cui, L. Ni, J. Jiang, Y. Pan, H. Wu, and Q. Chen, "Computational fluid dynamics simulation of thermal runaway reaction of styrene polymerization," *Organic Process Research Development*, vol. 23, no. 3, pp. 389–396, 2019, https://doi.org/10.1021/acs.oprd.9b00005.

[13] J. Jiang, H. Wu, L. Ni, and M. Zou, "CFD simulation to study batch reactor thermal runaway behavior based on esterification reaction," *Process Safety and Environmental Protection*, vol. 120, pp. 87–96, 2018, https://doi.org/10.1016/j.psep.2018.08.029.

[14] S. Jayanti, "Hydrodynamics of jet mixing in vessels," *Chemical Engineering Science*, vol. 56, no. 1, pp. 193–210, 2001, https://doi.org/10.1016/S0009-2509(99)00588-6.

[15] A. W. Patwardhan, "CFD modeling of jet mixed tanks," vol. 57, no. 8, pp. 1307–1318, 2002, https://doi.org/10.1016/S0009-2509(02)00049-0.

[16] H. D. Zughbi and M. A. Rakib, "Mixing in a fluid jet agitated tank: effects of jet angle and elevation and number of jets," *Chemical Engineering Science*, vol. 59, no. 4, pp. 829–842, 2004, https://doi.org/10.1016/j.ces.2003.09.044

[17] K. L. Wasewar, "A design of jet mixed tank," *Chemical and Biochemical Engineering Quarterly*, vol. 20, pp. 31–45, 2006.

[18] T. A. Oluwadero, C. Xuereb, J. Aubin, and M. Poux, "Effect of jet nozzle position on mixing time in large tanks," *Processes*, vol. 11, no. 7, p. 2200, 2023, https://doi.org/10.3390/pr11072200.

[19] E. Bumrungthaichaichan, N. Jaiklom, A. Namkanisorn, and S. Wattananusorn, "On the computational fluid dynamics (CFD) analysis of the effect of jet nozzle angle on mixing time for various liquid heights," *Scientific Research and Essays*, vol. 11, no. 4, pp. 42–56, 2016, https://doi.org/10.5897/SRE2015.6353.

[20] J. P. Torré, D. F. Fletcher, T. Lasuye, and C. Xuereb, "An experimental and CFD study of liquid jet injection into a partially baffled mixing vessel: A contribution to process safety by improving the quenching of runaway reactions," *Chemical Engineering Science*, vol. 63, no. 4, pp. 924–942, 2008, https://doi.org/10.1016/j.ces.2007.10.031.

[21] A. Kummer and T. Varga, "What do we know already about reactor runaway? – A review," *Process Safety and Environmental Protection*, vol. 147, pp. 460-476, 2021, https://doi.org/10.1016/j.psep.2020.09.059.

[22] J. Jiang, J. Jiang, Z. Wang, and Y. Pan, "Thermal runaway criterion for chemical reaction systems: A modified divergence method," *Journal of Loss Prevention in Process Industries*, vol. 40, pp. 199–206, 2016, https://doi.org/10.1016/j.jlp.2015.12.024.
[23] S. Wang, X. Peng, L. Jiang, and B. Li, "Investigation on the reaction characteristics and influencing factors of thermal runaway of di-tert-butyl peroxide," *Process Safety and Environmental Protection*, vol. 182, pp. 1185–1195, 2024, https://doi.org/10.1016/j.psep.2023.12.063.
[24] J. Jiang, Y. Chen, R. Zhou, and G. Mao, "CFD simulation study of thermal runaway inhibition for styrene polymerization by jet mixing," *Asia-Pacific Journal of Chemical Engineering*, vol. 19, no. 6, pp. 1–18, 2024, https://doi.org/10.1002/apj.3129.
[25] A. Milewska, and E. J. Molga, "CFD simulation of accidents in industrial batch stirred tank reactors," *Chemical Engineering Science*, vol. 62, no. 18-20, pp. 4920-4925, 2007, https://doi.org/10.1016/j.ces.2006.12.036.
[26] Y. T. Moon, H. Do Lee, and G. C. Park, "CFD simulation of steam jet-induced thermal mixing in subcooled water pool," *Nuclear Engineering and Design*, vol. 239, no. 12, pp. 2849–2863, 2009, https://doi.org/10.1016/j.nucengdes.2009.08.003.
[27] J. P. Torré, D. F. Fletcher, T. Lasuye, and C. Xuereb, "Single and multiphase CFD approaches for modelling partially baffled stirred vessels: Comparison of experimental data with numerical predictions," *Chemical Engineering Science*, vol. 62, no. 22, pp. 6246–6262, 2007, https://doi.org/10.1016/j.ces.2007.06.044.
[28] J. Zhu, T. Frerich, and A. S. Herrmann, "CFD modeling and validation of heat transfer inside an autoclave based on a mesh independency study," *Journal of Composite Material*, vol. 55, no. 18, pp. 2469–2487, 2021, https://doi.org/10.1177/0021998320979043.
[29] ANSYS Inc., "Ansys Fluent Theory Guide, Release 2025 R2," Canonsburg, PA: ANSYS Inc, 2025. [Online]. Available: http://www.ansys.com.
[30] J. Li, M. Wang, D. Fang et al., "CFD simulation on the transient process of coolant mixing phenomenon in reactor pressure vessel," *Annals Nuclear Energy*, vol. 153, p. 108045, 2021, https://doi.org/10.1016/j.anucene.2020.108045.
[31] ANSYS Inc., "Ansys Fluent User's Guide, Release 2025 R2," Canonsburg, PA: ANSYS Inc., 2025. [Online]. Available: http://www.ansys.com
[32] D. Lu, H. Wang, J. Chen, and Q. Su, "Flow and heat transfer experiment in a RPV with direct safety injection," *Nuclear Engineering and Design*, vol. 261, pp. 212–224, 2013, https://doi.org/10.1016/j.nucengdes.2013.03.022.
[33] R. K. Grenville and J. N. Tilton, "Jet mixing in tall tanks: Comparison of methods for predicting blend times," *Chemical Engineering Research and Design*, vol. 89, no. 12, pp. 2501–2506, 2011, https://doi.org/10.1016/j.cherd.2011.05.014.
[34] A. Patwardhan and S. G. Gaikwad, "Mixing in tanks agitated by jets," *Chemical Engineering Research and Design*, vol. 81, no. 2, pp. 211–220, 2003, https://doi.org/10.1205/026387603762878674.
[35] E. Bumrungthaichaichan, "A review on numerical consideration for computational fluid dynamics modeling of jet mixing tanks," *Korean Journal of Chemical Engineering*, vol. 33, pp. 3050–3068, 2016, https://doi.org/10.1007/s11814-016-0236-x.
[36] B. Kütük and İ. H. Güzelbey, "Computational fluid dynamics analyses of a VVER-1200 nuclear reactor vessel for symmetric inlet, asymmetric inlet, and LOCA conditions," *International Journal of Pressure Vessels and Piping*, vol. 187, p. 104165, 2020, https://doi.org/10.1016/j.ijpvp.2020.104165.